



Three-Dimensional Imaging-Based Radiobiological Dosimetry

George Sgouros, PhD, Eric Frey, PhD, Richard Wahl, MD, Bin He, PhD, Andrew Prideaux, PhD, and Robert Hobbs, PhD

Targeted radionuclide therapy holds promise as a new treatment for cancer. Advances in imaging are making it possible for researchers to evaluate the spatial distribution of radioactivity in tumors and normal organs over time. Matched anatomical imaging, such as combined single-photon emission computed tomography/computed tomography and positron emission tomography/computed tomography, has also made it possible to obtain tissue density information in conjunction with the radioactivity distribution. Coupled with sophisticated iterative reconstruction algorithms, these advances have made it possible to perform highly patient-specific dosimetry that also incorporates radiobiological modeling. Such sophisticated dosimetry techniques are still in the research investigation phase. Given the attendant logistical and financial costs, a demonstrated improvement in patient care will be a prerequisite for the adoption of such highly-patient specific internal dosimetry methods.

Semin Nucl Med 38:321-334 © 2008 Elsevier Inc. All rights reserved.

Systemically delivered radionuclide therapy of cancer may be accomplished by targeting the tumor itself,¹ the tumor-associated vasculature,² or the tumor-associated stroma.³ In each case, either because of the spatial distribution of the targets or the anatomic and physiological transport and penetration characteristics of the carrier, the spatial distribution of radionuclide within the tumor or normal organs is rarely uniform. Advances in imaging technology, accompanied by advances in image reconstruction and processing methodologies, as well as the availability of positron-emitting analogs of therapeutic radionuclides that allow PET imaging for therapy treatment planning, have made it possible to measure the nonuniformity in radionuclide distribution in patients. Currently, the resolution for nuclear medicine imaging is in the millimeter to centimeter range, which makes it possible to detect macroscopic nonuniformities in the activity distribution.

Such information, combined with information regarding tissue properties that may be obtained from anatomical imaging, makes it possible to perform dosimetry calculations that account for the nonuniformity in activity distribution

over time and space. In turn, this makes it possible to take a first tentative step toward providing a radiobiological interpretation of absorbed dose (and dose-rate) distributions. The objective of such an approach is to translate absorbed dose to tumor control or normal organ toxicity probability. In this work, we review recent advances in imaging-based 3-dimensional (3D) dosimetry that incorporate radiobiological modeling.

Overview of Imaging-Based Dosimetry Methods

Patient-specific, 3D image-based internal dosimetry involves using the patient's own anatomy and spatial distribution of radioactivity over time to obtain an absorbed dose calculation that provides as output the spatial distribution of absorbed dose. The results of such a patient-specific 3D imaging-based calculation can be represented as a 3D parametric image of absorbed dose, as dose-volume histograms over user-defined regions of interest or as the mean, and range of absorbed doses over such regions.⁴⁻¹⁰

A number of groups have pursued and contributed to 3D imaging-based patient-specific dosimetry.^{6,7,9,11-19} Several efforts used the basic MIRD formalism as applied to a standard phantom geometry.^{20,21} The standard phantom geometry was modified to include on-line Monte Carlo calculation and

The Russell H. Morgan Department of Radiology and Radiological Science, Johns Hopkins University, School of Medicine, Baltimore, MD.

Address reprint requests to George Sgouros, PhD, The Russell H. Morgan Department of Radiology and Radiological Science, 4M61 CRB II, 1550 Orleans St, Johns Hopkins University, School of Medicine, Baltimore, MD 21231. E-mail: gsgourol@jhmi.edu

therefore the ability to introduce tumors and adjust organ masses and shapes.

The software package, MABDOSE^{12,13} uses a 3D lattice in which to conduct radiation transport, scoring energy deposition in discrete voxels. The dosimetry system uses the same algorithm used by the MIRDOSE committee for photon transport, and assumes local deposition of particulate energy.

Clairand and coworkers described a dosimetry program, DOSE3D,¹⁵ which can be used to calculate dosimetric parameters for anthropomorphic phantoms defined with combinatorial geometry. DOSE3D allows the user to add spheres within the phantom for simulating tumors, to change the shape of one or more organs and, for organs defined by pair, to calculate individual dosimetric parameters for each organ. The program was validated for ¹³¹I and ^{99m}Tc by calculating S values for the Medical Internal Radiation Dose (MIRD) adult male phantom and comparing these results with data provided by MIRDOSE3 (now OLINDA²²⁻²⁴).

The software package, OLINDA/EXM, which implements the MIRD standard phantom-based methodology^{23,24} and is the nuclear medicine community standard for phantom-based dosimetry calculations, allows the user to adjust standard phantom organ masses and also includes a module for estimation of spherical tumor self-dose. Patient-specific dosimetry software that is not based on standard phantom geometries is briefly described in the paragraphs to follow.

The Royal Marsden Dosimetry Package (RMDP)¹¹ uses manual, marker-, or voxel-based registration to register images from different modalities and the sequence of single-photon emission computed tomography (SPECT) studies required for 3D dosimetry calculations. The 3D patient-specific dosimetry routines use either a beta-kernel or voxel S-factors. Phase-fitting each voxel's activity series enables more robust maps to be generated in the presence of imaging noise, such as is encountered during late, low-count scans or when there is significant redistribution within the volume of interest between scans. Error analysis can be applied to each generated dose-map. Patients receiving ¹³¹I-mIBG, ¹³¹I-NaI, and ¹⁸⁶Re-HEDP therapies have been analyzed with the use of RMDP. A Monte-Carlo package, developed specifically to address the problems of ¹³¹I quantification by including full photon interactions in a hexagonal-hole collimator and the gamma camera crystal, has been included in the dosimetry package.

A dosimetry tool called OEDIPE^{4,25,26} has been developed by the group at Nantes, France, to carry out personalized internal dosimetry calculations for nuclear medicine and for radiation safety (in the case of internal contamination). The software creates anthropomorphic voxel-based phantoms from computed tomography (CT) and magnetic resonance imaging (MRI) patient images through the use of a friendly graphical user interface. Several tools have been built-in to allow for image segmentation. Source data, including volume of interest localization and cumulated activities, are assessed by the use of SPECT images, and the source may be specified in any number of organs either as a point source or a homogeneously distributed source. It is also possible to choose the dosimetric parameters required for the study (mean organ dose or a dose distribution). Phantom, source, and dosimet-

ric parameters are automatically written into a file. That file is then processed by the Monte Carlo code MCNPX (LANL) to perform the actual dose calculation. OEDIPE can compute either the absorbed dose in each organ (in a few minutes), or the absorbed dose in each voxel of the phantom (ie, the spatial dose distribution at a tissue level) in a few hours or more. OEDIPE automatically reads the MCNPX output file and processes results to give a list of absorbed doses in each organ or a plot of isodose curves superimposed onto the phantom. Because of the long calculation times required to compute an absorbed dose within an entire whole-body phantom at a spatial resolution of a few millimeters, modifications were made to reduce computational times to reasonable values. More recently, this group has been investigating use of the GATE Monte Carlo code that is based on the GEANT4 Monte Carlo software libraries developed at CERN, the high-energy physics center in Geneva, Switzerland.^{27,28}

MINERVA, an extension of the external beam treatment planning package, PEREGRINE, developed at the Lawrence Livermore National Laboratory, has been used for internal dosimetry calculations.^{18,29-31} The goal of the MINERVA dose calculation system is to provide 3D Monte Carlo simulation-based dosimetry for radiation therapy, focusing on experimental and emerging applications. For molecular targeted radionuclide therapy applications, MINERVA calculates patient-specific radiation dose estimates using computed tomography to describe the patient anatomy, combined with a user-defined 3D radiation source. The new MINERVA system will ultimately incorporate capabilities for a comprehensive list of radiation therapies, including boron neutron capture therapy, brachytherapy and proton therapy. Using the open application programming interface, other groups can add their own modules and share them.

The DOSIMG software⁹ has been used with mathematical anthropomorphic phantoms to examine the impact of different quantitative SPECT algorithms on Monte Carlo-derived absorbed dose calculations. Mathematical phantom-derived CT and SPECT images were generated, and dose calculations derived from these were compared with "true" dose results derived from the actual mathematical phantom data.³² The SPECT quantitation methodologies derived from this work were subsequently applied to ¹¹¹In/90Y dosimetry.³³

The earliest 3D imaging-based targeted radionuclide dosimetry package described in the literature³⁴ was heavily influenced by treatment planning techniques developed for external radiotherapy treatment planning.³⁵ The 3D-ID (3D-internal dosimetry) software package takes the distribution of radionuclide for a given patient (eg, from SPECT or positron emission tomography [PET]) and combines it with anatomical information (eg, CT or MRI) to yield absorbed dose estimates that are specific to a particular patient's biodistribution and anatomy.^{7,10,34,36-38} This work introduced the concept of dose-volume histograms for internally administered radionuclides.³⁹ The software package, 3D-ID, may be used to conduct both Monte Carlo and point-kernel-based calculations. It has been used to examine the impact of different radionuclides on the dose distribution, given a fixed cumulated activity distribution.⁶ 3D-ID has been used to perform a

detailed analysis of tumor dose versus response in the treatment of patients with non-Hodgkin's lymphoma by using ^{131}I -anti-B1 antibody.³⁸ The point-kernel module in 3D-ID, and data from a clinical trial of ^{131}I -labeled anti-B1 antibody were used. More recently, 3D-ID has been used in thyroid cancer patients using ^{124}I PET imaging data with CT for tumor dosimetry.⁴⁰ This study demonstrated use of multiple PET image studies which were registered across time and integrated, voxel-by-voxel, to provide a 3-D cumulated activity image used in the dosimetry calculation. The same data set and general approach was also used to perform normal organ dosimetry.⁴¹ A next-generation version of 3D-ID, named 3D-RD for 3D radiobiological dosimetry,⁴² has been developed that incorporates radiobiological modeling. 3D-RD is described in detail in the section "Imaging-based 3D Radiobiological Modeling."

Quantitative Imaging Input

Accurate imaging-based dosimetry requires accurate quantitative imaging information. In PET, the imaging data are typically corrected for scatter and attenuation by the use of camera vendor software. Depending on the characteristics of the positron-emitting radionuclide, additional corrections may be required.⁴³ In SPECT, a number of corrections are needed. A tremendous amount of work has been performed in this area, and readers are referred to recent books in this area^{44,45} as well as to a number of key individual contributions.⁴⁶⁻⁵⁷ The work of Frey and coworkers in this area is described in this article.⁵⁸⁻⁶⁴

Physical phantom experiments using ^{111}In in the RSD torso phantom and Monte Carlo simulation experiments simulating ^{111}In in the NonUniform Rational B-Spline (NURBS)-based cardiac torso (NCAT) phantom^{65,66} have been used to evaluate quantitative imaging. In the physical phantom experiment, activities were placed in the heart, lungs, liver, and background with activity concentration ratios of 19:5:20:1. Two spherical lesions with diameters 25 mm and 35 mm were placed in the phantom. The spheres had activity concentrations relative to the background of 20:1 for the larger sphere and 110:1 for the smaller. The total activity used was 5 mCi. A GE Millenium VH SPECT system with Hawkeye x-ray CT, a 1"-thick crystal and a MEGP collimator were used for data acquisition. Planar whole-body anterior and posterior images were obtained with a pixel size of 2.2 mm. SPECT projections were acquired into 128×128 matrices with a 4.4-mm pixel size at 180 views over 360° with the use of 2

14% wide energy windows centered at 171 and 245 keV. The SPECT acquisitions were followed by a radiograph CT scan. Two SPECT studies were performed, one covering the upper part of the phantom and one the lower part. Long acquisitions were used to obtain low noise data. A calibration image using a syringe containing 18.5 MBq (500 μCi) of ^{111}In was also obtained.

The projections were reconstructed with OSEM reconstructions with compensation for various combinations of attenuation (A), scatter (S), Geometric Response Function (G), and Collimator-Detector Response Function (D).⁶² Regions of interest (ROIs) around the various organs were manually defined with the SPECT and CT slices. For the spheres, the axial resolution was insufficient to draw accurate ROIs; therefore, spherical ROIs were created with the correct size and aligned with the centers of the lesions. For the planar studies, ROIs were drawn manually and made smaller than the actual organs to avoid overlap. For the SPECT, the reconstructed pixel values were converted to activity concentration using the calibration factor. For the planar studies, TEW scatter compensation was performed before computing the geometric mean. The geometric mean values were converted to activity using a scale factor based on the whole body geometric mean counts and the known activity in the phantom. Relative error in the total activity in each ROI was determined and the results are shown in Table 1 (negative signs indicate underestimation compared with the true activity).

Note that, with full compensation, the quantitative accuracy for SPECT was relatively good. Accuracy was greatly improved by the addition of attenuation and scatter compensation and, for the case of the spheres, geometric response function compensation. For ^{111}In and this particular collimator, collimator-detector response function (CDRF) compensation provided only modest improvements. This likely is a result of the fact that the collimator penetration and scatter fraction is only about 11% and is relatively independent of distance. Thus, the calibration procedure effectively accounted for collimator effects. Also note that planar imaging is generally worse than the SPECT methods, especially for the spheres and the lung region.

A simulation experiment for a single phantom anatomy and biodistribution was performed to further demonstrate the efficacy of the corrections outlined already. In this study, the NURBS-based cardiac torso (NCAT) phantom (Fig. 1) was used as a model of human anatomy. The SimSET Monte Carlo (MC) simulation code (University of

Table 1 Relative Error in Organ Activities for SPECT with Various Compensations and Planar Imaging

Method	Heart	Lung	Liver	Large Sphere	Small Sphere
OSEM-NC	-75.56%	-62.06%	-70.78%	-74.76%	-78.22%
OSEM-A	31.73%	38.49%	42.79%	-1.11%	-11.75%
OSEM-AS	-8.36%	-1.60%	0.04%	-20.30%	-22.42%
OSEM-AGS	-4.58%	3.34%	4.65%	-2.38%	3.85%
OSEM-ADS	-5.22%	2.48%	4.11%	0.74%	9.06%
Planar	-5.16%	18.9%	-2.51%	14.5%	-21.3%

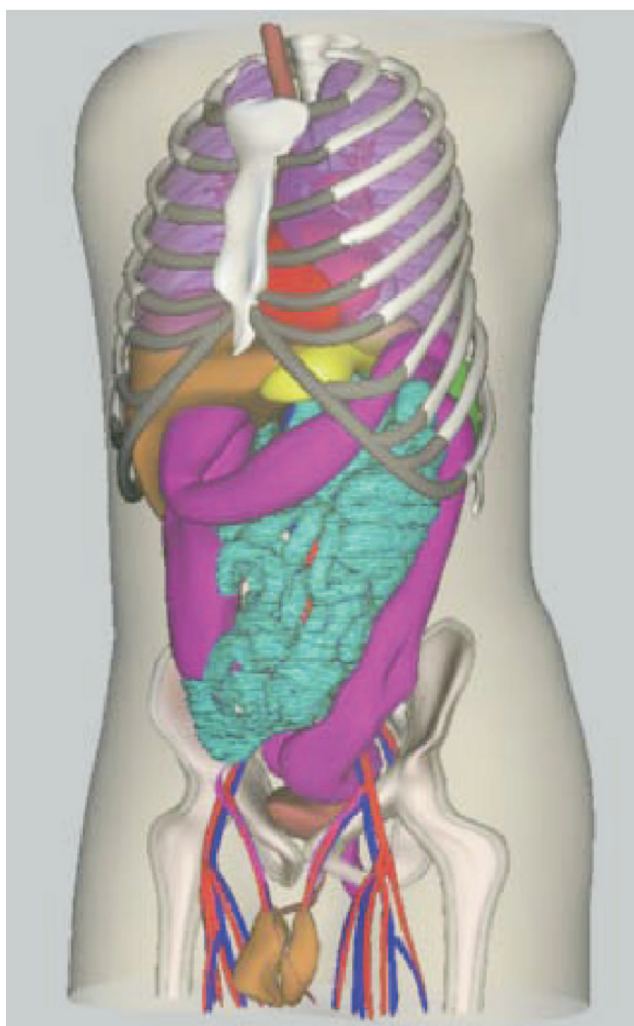


Figure 1 Depiction of the nonuniform rational b-splines (NURBS) NCAT mathematical phantom.

Washington⁶⁷) combined with a method for modeling the CDRF was used for imaging simulation.⁶⁸ Noise modeling was neither clinically realistic nor Poisson distributed. Projection data of the kidneys, liver, and the remainder of the body (including lungs, heart, pelvic marrow, large blood vessels in the chest and abdomen, and spleen) were separately generated. A GE VG camera with 1" crystal and a medium-energy general-purpose (MEGP) collimator was simulated. Both ¹¹¹In photopeaks were simulated. The up-

take in the liver, lungs, blood, bone marrow, kidneys, spleen, and body at 0 hours was based on the values determined from a patient study using Zevalin.⁶⁹ Each organ, and the body individually, were then scaled to model the observed kinetics for that organ.

With the use of this procedure, both simulated SPECT and anterior and posterior planar datasets at 0, 5, 24, 72, and 144 hours after injection were generated. The SPECT images were reconstructed with ordered-subsets expectation maximization (OSEM) with no compensation (NC) and with (Attenuation, Collimator-Detector Response Function and Scatter) ADS compensation. The images (see Fig. 2) were also reconstructed with an ordered subsets MAP (OSMAP) algorithm with ADS compensation with a prior that penalizes deviations from the region mean in the major blood vessels, marrow, heart, lungs, liver, kidneys, and spleen. For the OSMAP reconstructions, the true regions were used as the regions in which to enforce the prior (the region means were estimated during the reconstruction).

Note the good resolution in the OSEM-ADS images compared with OSEM-NC, which is attributable to the CDRF compensation. The last 3 images in Fig. 2 are from the OSMAP-ADS reconstruction. Note that the intensity inside the organs is very uniform and that the degree of uniformity is controlled by the prior. Also note that the edges are very sharp. Furthermore, the background region is not smooth, because the prior was not applied in this region.

By using these simulated images, we integrated the exponential clearance curve in each organ. This was done both for conjugate-view planar (C-Planar) and Q-Planar, a planar quantitation method wherein scatter and attenuation are corrected by Monte Carlo modeling using CT images to define organ anatomy and composition.^{70,71} OSMAP-ADS (with $\beta = 0.1$) reconstruction was used to obtain Q-SPECT. Also, planar/SPECT methods where the half-life was determined from the planar images and the fraction of injected activity at time zero was determined by extrapolating the fraction of injected activity for the 24-hour SPECT image back to time zero were used. The resulting residence times were compared with the true values and the results are shown in Table 2. Note that, once again, negative values represent underestimates. The SPECT residence times for the planar/SPECT method were generally good compared with those from the purely planar method, but there were still significant discrepancies.



Figure 2 The leftmost image is the coronal slice through NCAT phantom with activity distribution modeling an ¹¹¹In Zevalin distribution at 24 hours. The second image to the right is the simulated anterior planar image from the same time point. The right 5 images are the same coronal slice as the phantom but reconstructed using OSEM-NC, OSEM-ADS, OSMAP-ADS with $\beta = 0.1$; OSMAP-ADS with $\beta = 0.01$; and OSMAP-ADS with $\beta = 0.001$.

Table 2 Relative Error in Estimated Residence Time for Planar and SPECT

Residence Time (h)	Heart	Lung	Liver	Kidney	Spleen	Marrow	Vessels
C-planar	20 ± 2%	-2 ± 0.8%	29 ± 1%	-21 ± 3%	-12 ± 1%	-24 ± 1%	-36 ± 1%
Q-planar	-6.5 ± 1%	10 ± 1%	-4 ± 1%	-7 ± 3%	-5 ± 3%	-1 ± 2%	-3.5 ± 3%
Q-SPECT	-3.6 ± 0.5%	2 ± 0.8%	-4.6 ± 0.4%	-5 ± 1%	-3 ± 1%	-0.5 ± 0.8%	6.4 ± 0.8%
C-planar/Q-SPECT	-9 ± 1%	-10 ± 0.8%	-8 ± 0.7%	-21.5 ± 3%	-17 ± 3%	-18 ± 1.3%	-9 ± 2%
Q-planar/Q-SPECT	-5 ± 1%	-0.6 ± 1%	-5 ± 1%	-3 ± 0.5%	-2.5 ± 3%	-0.5 ± 2%	5 ± 3%

The results of this simulation study indicate improved accuracy of quantitative SPECT methods as compared with planar and even planar/SPECT methods in estimating the residence times. Because the residence times are directly related to organ dose estimates, the organ dose estimates will be similarly better. These data also point out that the accuracy of planar imaging-based methods commonly used depends strongly on patient-specific factors. Improved planar methods or the use of quantitative SPECT are required to obtain more accurate organ dose estimates.

The efficacy of SPECT with compensation for physical image degrading factors in obtaining quantitative activity estimates for ^{131}I imaging has also been investigated. The same phantom (including the same relative organ activities) as in the ^{111}In analysis, above, was used. To highlight the power of iterative reconstruction approaches that simulate the collimator and detector response physics, collimators having thinner septa than traditionally used for ^{131}I imaging were also included in the study. The simulations were performed using low-energy, high-resolution (LEHR), MEGP, and high-energy general-purpose (HEGP) collimators. To reduce simulation time, only the 364 keV photon (and not higher energy photons) was modeled; noise was not included.

The noise characteristics of CDRF compensation were also investigated. To do this, the counts in the HEGP image were scaled so that the number of geometrically collimated photons was at the same count level as for clinical ^{111}In Zevalin images and simulated Poisson noise. For the other collimators, the projection data were scaled by the same factor as for the HEGP images times the relative sensitivity of the collimator with respect to the HEGP collimator. Thus, the total number of counts in the LEHR projection data was greater by a factor of more than 70. However, CDRF compensation was shown to require more iterations and the CDRF deconvolution resulted in noise amplification. This result is illustrated in the last row of images in Fig. 3. Note that the noise is clearly greater in the LEHR image, resulting from noise amplification during CDRF and the need to use 100 iterations.

From Fig. 3, we see that, despite the very poor quality of the LEHR projections, the reconstructed image with ADS is quite good. The image quality for both the MEGP and HEGP images was also significantly improved by ADS compared with AGS. Also, note that the use of OSMAP results in images with very good resolution and very sharp edges. Table 3 shows the relative errors in the organ activity estimates using the images obtained with these different collimators and

compensation methods. The perturbation-based geometric transfer matrix-based partial volume compensation (PVC) was also applied and the results are shown. For the LEHR collimator, 100 iterations were used while 20 were used for the MEGP and HEGP collimators. Note that, despite the very poor projection image, the ADS reconstruction for the LEHR collimator has relatively good quantitative accuracy, especially compared with the abysmal accuracy with AGS, indicating the potential efficacy of CDRF compensation. Also note that, despite significantly greater levels of penetration and scatter, the MEGP collimator provides, in general, more accurate quantification.

These data also demonstrate the importance of PVC: the use of either the perturbation-based geometric transfer matrix method or OSMAP resulted in significantly improved quantitative accuracy, especially for small structures like the blood and bone marrow, but also for organs like the spleen that are near organs with high uptake (such as the blood or heart). In the columns that include a “±,” the values are the mean and standard deviation over 50 realizations of noisy projections. As indicated by the noise in the image, the activity estimates from the LEHR collimator are less precise than those for the MEGP or HEGP collimators despite having ~70 times more counts. For the MEGP and HEGP collimators, the precisions are similar. Though these results are not for an optimal number of iterations they are suggestive that the choice of collimators with thick septa for ^{131}I imaging is not as obvious when the goal is accurate quantification and when CDRF compensation is used.

The question of quantification of structures of different sizes was examined by introducing spheres of different diameters in the femoral and inguinal regions of the phantom (Fig. 4). The results were generated with OSEM-ADS, with and without PVC; 20 iterations with 8 subsets per iteration were used. The pixel and bin size were 0.442 cm. HEGP collimation was simulated; the phantom was $128 \times 128 \times 200$. One-hundred twenty 128^2 projections spanning 360° were collected. The phantom organ activity concentration was chosen to match that of a recent NHL imaging simulation study⁷²: background = 4; blood = 48; bone marrow = 4; heart = 48; kidneys = 80; liver = 28; lung = 28; spleen = 52; tumor = 100. The results show 20% to 30% quantitative accuracy when the lesion size is >2.5 cm and results are obtained without PVC. Partial volume correction leads to a 5 to 10% overestimate of the activity. Because of the lower photon energy and reduced scatter, ^{111}In images are expected to yield better results for small lesions.

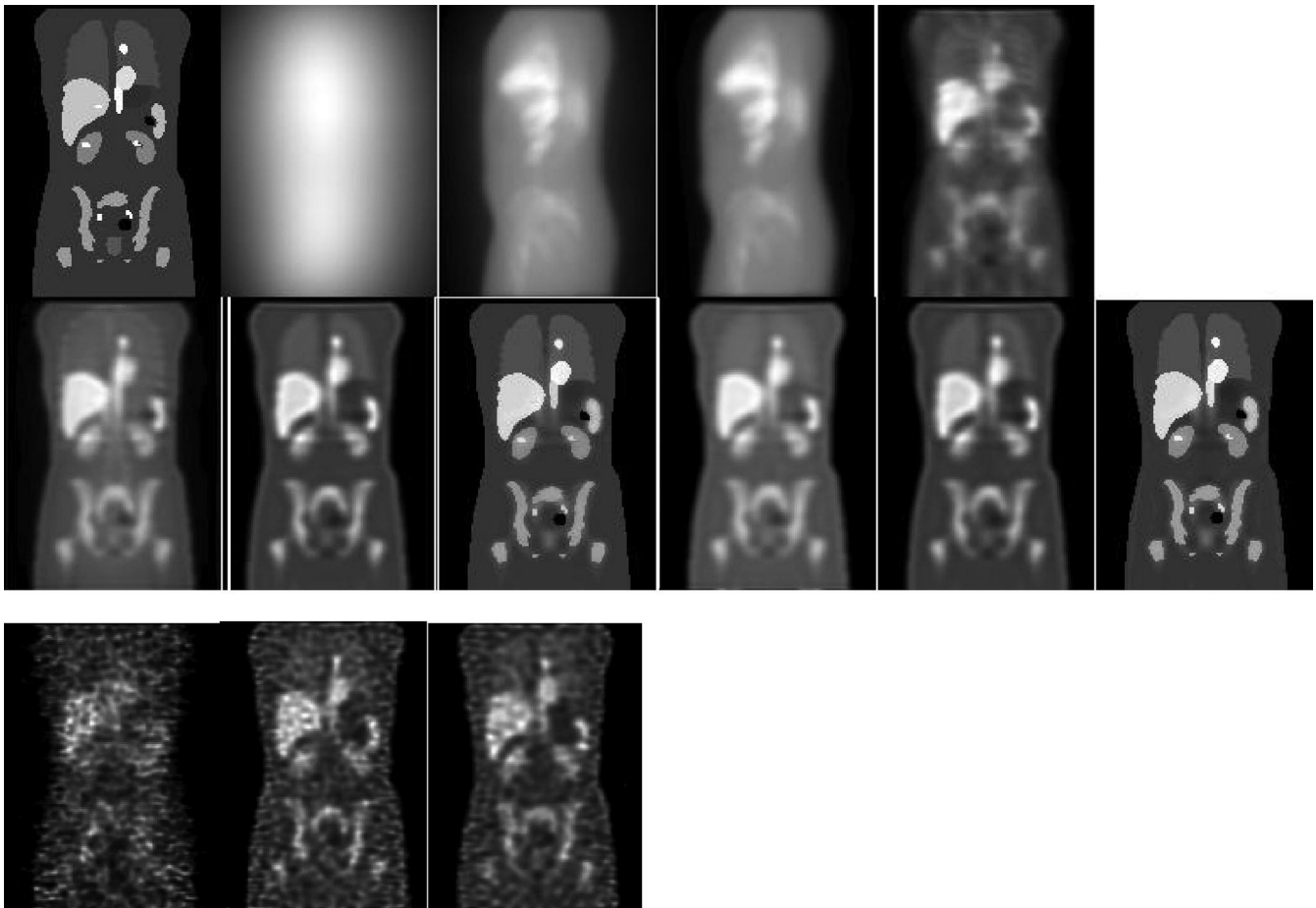


Figure 3 Top row, left to right: coronal slice through phantom; left lateral projection with LEHR collimator; left lateral projection with MEGP collimator; left lateral projection with HEGP collimator; coronal SPECT reconstruction with LEHR collimator and ADS compensation (100 iterations of OSEM with 8 subsets). Middle row, left to right, SPECT reconstructions from 20 iterations of: MEGP and OSEM-AGS; MEGP and OSEM-ADS; MEGP and OSMAP-ADS; HEGP and OSEM-AGS; HEGP and OSEM-ADS; HEGP and OSMAP-ADS. Bottom row, left to right, reconstructions from noisy projections using same number of iterations as for noise-free images: LEHR and OSEM-ADS; MEGP and OSEM-ADS; HEGP and OSEM-ADS.

Radiobiological Modeling

Accurate, detailed absorbed dose calculations are useful only to the extent that they are biologically relevant and easily interpretable. The uniformity (or lack thereof) of absorbed dose distributions and their biological implications has been examined intensively, primarily in animal studies, however.⁷³⁻⁸¹ To address the question of how to best represent the large amount of data in 3D distributions of absorbed dose, one may look to the radiotherapy field and use dose-volume histograms to represent dose distributions in targeted radionuclide therapy.³⁹

Equivalent Uniform Dose (EUD)

The EUD model takes this one step farther by introducing the radiobiological parameters, α and β , the sensitivity per unit dose, and per unit dose squared in the linear-quadratic dose-response model to convert the spatially varying absorbed dose distribution into an equivalent uniform absorbed dose value that would yield a biological response

similar to the one expected from the original dose distribution. This provides a single value that may be used to compare different dose distributions; the value also reflects the likelihood that the magnitude and spatial distribution of the absorbed dose is sufficient for tumor kill. The concept (and value) of EUD is illustrated by considering a tumor in which one-half of the volume receives a dose of 100 Gy and the other half receives 0 Gy. Such an absorbed dose distribution would lead to treatment failure since the tumor half not exposed to radiation would re-grow. In this case the absorbed dose delivered uniformly throughout the tumor volume (ie, the EUD) would be close to zero to be consistent with the expected biological effect of the dose distribution described above. The illustration should also make it clear that EUD is not valid for normal organs since normal organs have a structural organization (ie, 100 Gy to even a small portion of the spine can lead to paralysis; in contrast, 100 Gy to a large portion of the liver may be inconsequential since the liver can regenerate). Calculation of EUD requires knowledge of the radiosensitivity of

Table 3 Relative Error (in %) in Organ Activity Estimates for the 3 Collimators and Various Reconstruction Methods

Organ/ROI	LEHR Collimator			MEGP Collimator			HEGP Collimator			
	OSEM ADS	OSEM AGS	OSEM	OSEM ADS PVC	OSMAP ADS	OSEM AGS	OSEM ADS PVC	OSMAP ADS	OSEM AGS	
Blood	-60.2 ± 1.1	1704		-41.9 ± 0.51	-9.67 ± 0.84	-24.63	-14.43	-44.6 ± 0.52	-25.17	-35.43
Marrow	-37.5 ± 1.4	3343		-19.6 ± 0.50	-1.08 ± 0.61	-8.48	32.60	-20.7 ± 0.47	-8.09	-0.63
Heart	-12.1 ± 0.98	2545		-8.66 ± 0.37	-0.53 ± 0.41	-0.97	48.05	-9.24 ± 0.28	-0.64	18.24
Kidney	-19.9 ± 2.7	4384		-10.9 ± 0.85	2.1 ± 0.99	-2.71	55.19	-11.4 ± 0.90	-2.11	15.67
Liver	-7.5 ± 0.55	2927		-5.60 ± 0.22	-0.22 ± 0.24	0.09	56.46	-5.98 ± 0.25	0.34	24.03
Lung	6.6 ± 1.2	5100		1.46 ± 0.37	6.60 ± 0.42	-0.15	88.03	1.98 ± 0.36	0.30	39.41
Spleen	-25.6 ± 2.4	2378		-12.9 ± 0.64	-0.56 ± 0.73	-7.30	31.74	-13.4 ± 0.64	-7.69	7.25

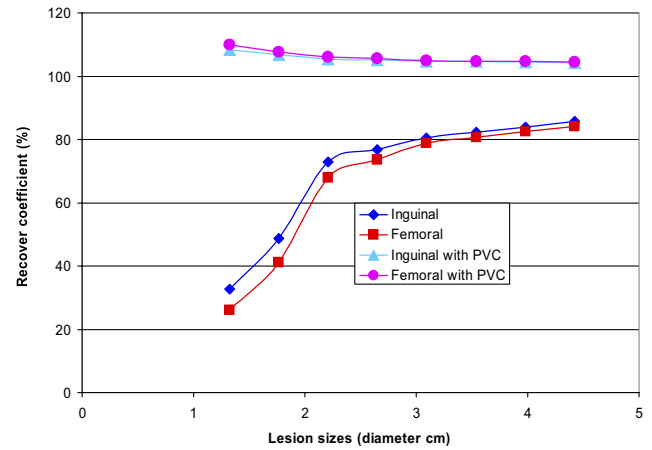


Figure 4 Recovery coefficient as a function of lesion size for 2 lesions placed at the inguinal and femoral vessels. The effect of PVC is illustrated. (Color version of figure is available online.)

the tumor and the assumption that all elements of the tumor are clonogenic. As is well-recognized, the radiosensitivity is likely to vary in different tumor regions (eg, hypoxic versus normoxic). Clonogenicity, likewise, will be variable throughout the tumor (ie, dormant versus rapidly proliferating regions). Nevertheless, EUD is still potentially useful in comparing different tumor absorbed dose distributions in a patient trial population.

Biologically Effective Dose (BED)

That dose rate influences response has been known for several decades.⁸² The BED formalism,^{83,84} initially termed extrapolated response dose (ERD), was developed to compare different fractionation protocols for external radiotherapy. BED may be thought of as the actual physical dose adjusted to reflect the expected biological effect if it were delivered at a reference dose rate. As in the case of EUD, by relating effects to a reference value, this makes it possible to compare doses delivered under different conditions. In the case of EUD, the reference value relates to spatial distribution and is chosen to be a uniform distribution. In the case of BED, the reference value relates to dose rate and is chosen to approach zero (total dose delivered in an infinite number of infinitesimally small fractions). In radionuclide therapy, the dose rate varies temporally, and a number of investigators have examined the implications of this on tumor control and normal tissue toxicity.⁸⁵⁻⁹² Motivated by the desire to incorporate internal emitter dosimetry in conjunction with external beam radiotherapy, the group at the Royal Marsden first implemented voxel-based BED calculations to account for the difference in dose-rate between radionuclide therapy and external beam radiotherapy and to present BED maps.^{93,94}

The rationale for incorporating BED into imaging-based dosimetry software such as 3D-RD is also driven, in part, by the use of engineered, lower molecular weight targeting agents (peptides and single-chain constructs), by multistep targeting approaches,⁹⁵⁻¹⁰⁰ and by bone-seeking agents.¹⁰¹⁻¹⁰³ The targeting and excretion kinetics of these agents differ

substantially and, as suggested by preclinical and clinical evidence,^{92,104-107} the dose rate at which a total dose is delivered may become an important parameter in understanding normal organ toxicity and tumor response. To date, almost all clinical studies have considered only total absorbed dose, the majority of which is delivered at an exponentially decreasing dose rate. In contrast, the benchmark for projecting potential toxicity and justifying initial phase I activity and absorbed dose levels has been the experience with normal organ tolerance in external beam radiotherapy. However, in external beam therapy, the absorbed dose is typically delivered at high dose-rate in daily 2-Gy fractions over a period of 30 to 40 days. In the simplest and more generally applied BED model knowledge of three tissue-specific parameters: α , β , and μ , an estimate of the repair rate (assuming exponential repair) following tissue damage is required.

Imaging-Based 3D Dosimetry

3D imaging-based dosimetry entails the following steps: (1) Input a series of longitudinal 3-D SPECT/CT or PET/CT images. (2) Register the images across time by using both the SPECT or PET data set and the corresponding CT set. (3) Obtain the cumulated activity for each voxel either by fitting an exponential function to each voxel and integrating analytically over time or by performing a numerical integration over time for each voxel.⁴⁰ (4) Use the CT image voxel values to assign density and composition (ie, water, air and bone).^{6,108} (5) Use the 3-D cumulated activity image and the matched density and composition image to perform a Monte Carlo calculation to estimate the absorbed dose by tallying energy deposition in each voxel.⁶ (6) Present the absorbed dose distribution as a set of images, isodose contour plots, or as dose volume histograms for user-identified tumor or normal organ volumes.

Imaging-based 3D Radiobiological Modeling

To introduce radiobiological modeling, the steps described in the previous section are modified so that absorbed dose-rate images are calculated for each time-point rather than for a cumulated activity map. To obtain the total absorbed dose the individual dose-rate images are integrated over time to yield images of absorbed dose. The individual absorbed dose rate images may also be interpreted as absorbed dose images reflecting the absorbed dose delivered over the imaging time-period. By fitting these images voxel by voxel to an exponential function, an image of absorbed dose rate may be obtained. This information, coupled with assignment of the radiobiological parameters, α , β , μ , the radiosensitivity per unit dose, radiosensitivity per unit dose squared and the repair rate assuming an exponential repair process, respectively,^{109,110} can be used to generate a BED value for each voxel, and subsequently an EUD value for a particular user-defined volume.

In external radiotherapy, the expression for BED is as shown:

$$BED = Nd \left(1 + \frac{d}{\alpha/\beta} \right) \quad (1)$$

In this equation, N is the number of fractions given of absorbed dose, d , delivered over a time interval that is negligible relative to the repair time for radiation damage (ie, at high dose rate) where the interval between fractions is long enough to allow for complete repair of repairable damage induced by the dose d ; repopulation of cells is not considered in this formulation. The parameters, α and β are the coefficients for radiation damage proportional to dose (single event is lethal) and dose squared (two events required for lethal damage), respectively. A more general formulation of eq 1 is shown in eq 2¹¹¹:

$$BED(T) = D_T(T) \cdot RE(T), \quad (2)$$

where $BED(T)$ is the biologically effective dose delivered over a time T , $D_T(T)$ is the total dose delivered over this time, and $RE(T)$ is the relative effectiveness per unit dose at time T . The general expression for $RE(T)$ assuming a time-dependent dose rate described by $\dot{D}(t)$ is given by eq 3:

$$RE(T) = 1 + \frac{2}{D_T(T) \left(\frac{\alpha}{\beta} \right)} \times \int_0^T dt \cdot \dot{D}(t) \int_0^t dw \cdot \dot{D}(w) e^{-\mu(t-w)}. \quad (3)$$

The second integration over the time-parameter, w , represents the repair of potentially lethal damage occurring while the dose is delivered, ie, assuming an incomplete repair model.¹¹² If we assume that the dose rate for radionuclide therapy, $\dot{D}(t)$ at a given time, t , can be expressed as an exponential expression:

$$\dot{D}(t) = \dot{D}_0 e^{-\lambda t}, \quad (4)$$

where \dot{D}_0 is the initial dose rate and λ is the rate at which the absorbed dose decreases ($= \ln(2)/t_e$; t_e = the half-life associated with the absorbed dose decrease), then, in the limit, as T approaches infinity, the integral in eq 3 reduces to:

$$\frac{\dot{D}_0^2}{2\lambda(\mu - \lambda)}. \quad (5)$$

Substituting this expression and replacing $D_T(T)$ with D , the total dose delivered, and using $\dot{D}_0 = \lambda D$, which may be derived from eq 4, we get:

$$BED = D + \frac{\beta D^2}{\alpha} \left(\frac{\ln(2)}{\mu \cdot t_e + \ln(2)} \right). \quad (6)$$

In this expression, the dose rate parameter, λ , is represented by $\ln(2)/t_e$. The derivation follows closely that described by Dale and coworkers.¹⁰⁹

In cases in which the absorbed dose rate in a particular voxel is not well fitted by a single decreasing exponential, alternative formalisms have been developed that account for

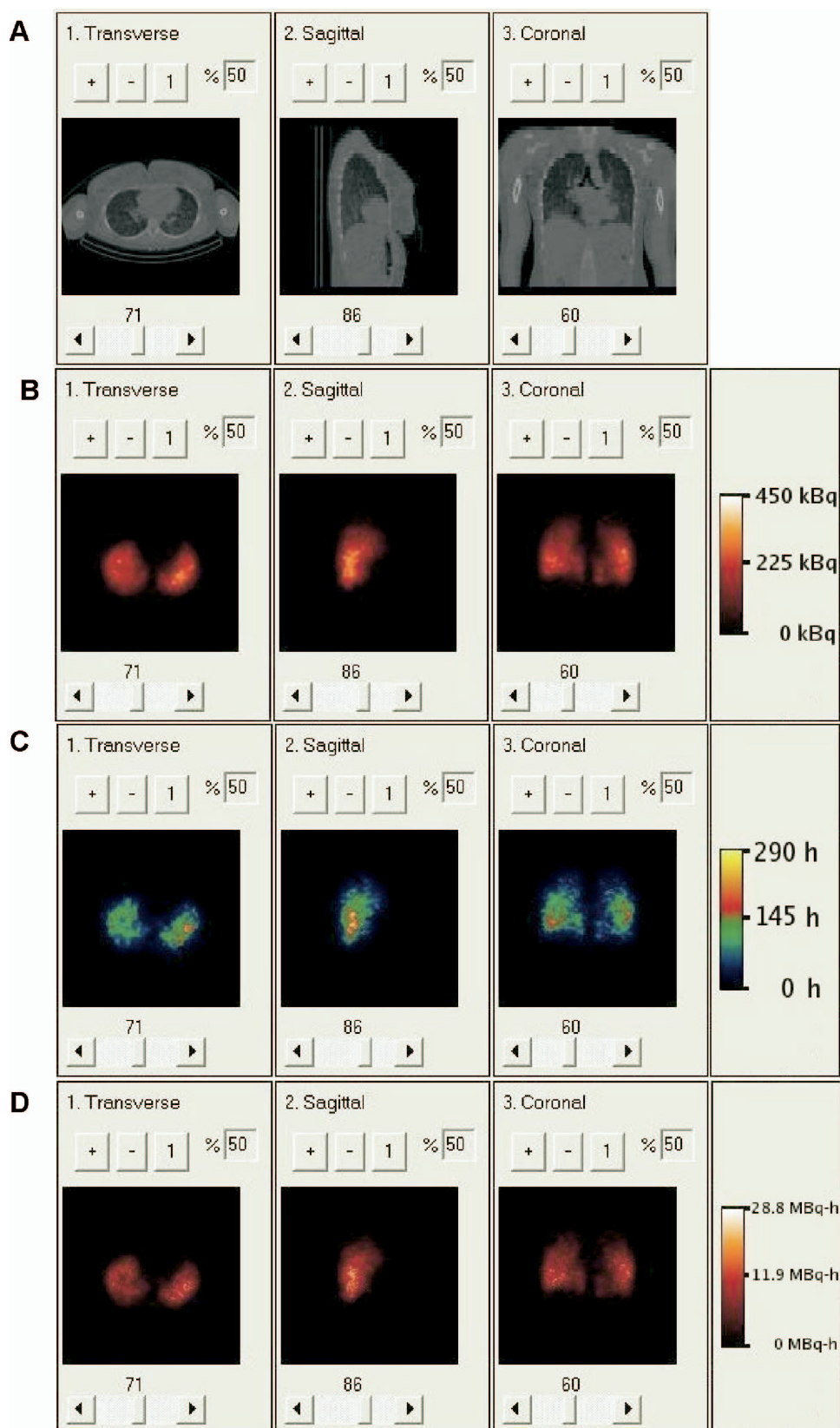


Figure 5 (A) Clinical CT of patient showing nonuniform density distribution in lungs. (B) Clinical SPECT of patient showing nonuniform activity distribution. (C) Rate map generated from 3 longitudinally aligned SPECT images; regions with effective half-life greater than the physical half-life of ^{131}I reflect tumor uptake. (D) Cumulative activity image generated from rate map and SPECT.

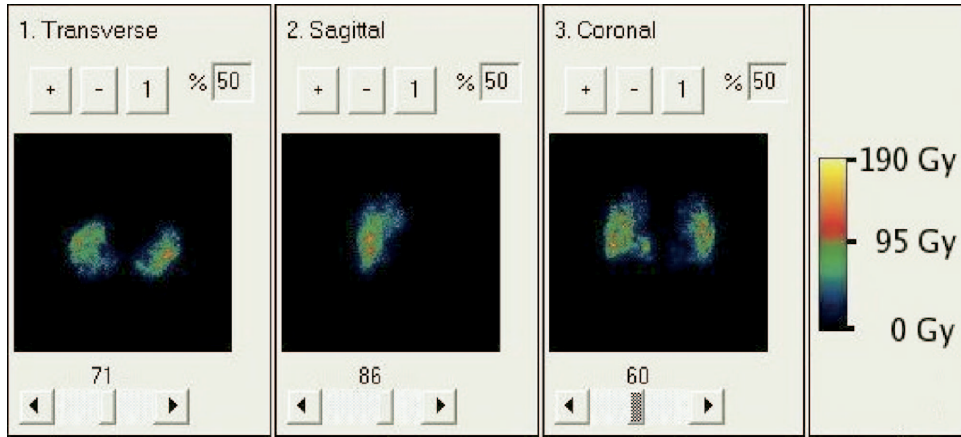


Figure 6 BED map resulting from 3D-RD using full patient specific data. Although the values of absorbed dose and BED are different, their relative changes from voxel to voxel are so similar that it is nearly impossible to visually differentiate the two.

an increase in the dose rate followed by exponential reduction. Since the number of imaging time-points typically collected in dosimetry studies would not resolve a dual parameter model (ie, uptake and clearance related dose-rate changes) the current methodology assumes that the total dose contributed by the rising portion of a tissue or tumor time-activity curve is a small fraction of the total absorbed dose delivered.

Eq 6 depends on the tissue-specific intrinsic parameters α , β , and μ . These 3 parameters are set constant throughout a user-defined organ or tumor volume. The voxel specific parameters are the total dose in a given voxel and the dose-rate assigned to the voxel (represented by the corresponding half-time). Given a voxel at coordinates (i,j,k) , D^{ijk} and t_e^{ijk} are the dose and half-time associated with the reduction in absorbed dose over time for the voxel. The imaging-based formulation of expression 6 that is incorporated into a 3D radiobiological dosimetry is then:

$$BED^{ijk} = D^{ijk} + \frac{\beta D^{ijk^2}}{\alpha} \left(\frac{\ln(2)}{\mu \cdot t_e^{ijk} + \ln(2)} \right). \quad (7)$$

The user inputs values of α , β , and μ for a particular volume and D^{ijk} and t_e^{ijk} are obtained directly from the 3D dose calculation and dose rate image, respectively. This approach requires organ or tumor segmentation that corresponds to the different α , β , and μ values. The dose values are obtained by Monte Carlo calculation as described previously,⁶ and the effective clearance half-lives are obtained by fitting the data to a single exponential function, as has been previously described.¹⁰ Once a spatial distribution of BED values has been obtained a dose-volume histogram of these values can be generated. Normalizing so that the total area under the BED (differential) DVH curve is one, one converts the BED DVH to a probability distribution of BED values denoted, $P(\psi)$, where ψ takes on all possible values of BED. Then, following the derivation for EUD from reference,⁷⁴ the EUD is obtained as:

$$EUD = -\frac{1}{\alpha} \ln \left(\int_0^{\infty} P(\psi) e^{-\alpha \psi} d\psi \right). \quad (8)$$

The EUD of the absorbed dose distribution, as opposed to the BED distribution, can also be obtained using eq 8, but using a normalized DVH of absorbed dose values rather than BED values. Eq 8 may be derived by determining the mean absorbed dose required to yield a surviving fraction equal to that arising from the probability distribution of dose values (absorbed dose or BED) given by the normalized DVH.

The voxel-based methodology outlined above has also been applied at the organ level and formulated to be consistent with the MIRD organ-level S-value dosimetry schema.¹¹³

Implementation of 3D Imaging-Based Radiobiological Modeling

Results from a 3D imaging-based radiobiological modeling analysis obtained using an early version of the software package, 3D-RD,¹¹⁴ in which activity kinetics were used in place of absorbed dose kinetics for the radiobiological modeling are illustrated below. The 3D-RD dosimetry methodology was applied to the case of an 11-year-old female thyroid cancer patient who has been previously described in a publication on MCNP-based 3D-ID dosimetry.

SPECT/CT images were obtained at 27, 74, and 147 hours after injection of a 37-MBq (1.0 mCi) tracer ¹³¹I dose. All 3 SPECT/CT images focused on the chest of the patient, and close attention was directed at aligning the patient identically for each image. The images were acquired with a GE Millennium VG Hawkeye system (Milwaukee, WI) with a 1.59-cm thick crystal.

An OSEM-based reconstruction scheme was used to improve quantization of the activity map.¹¹⁵ A total of 10 iterations with 24 subsets per iteration was used. This reconstruction accounts for effects, including attenuation, patient

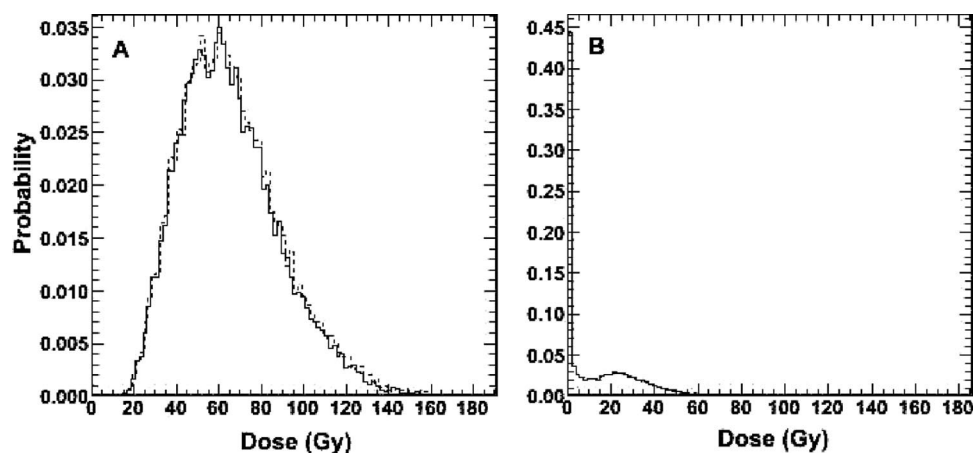


Figure 7 (A) Differential absorbed dose (solid line) and BED-volume-histogram (dashed line) for tumor. (B) differential BED-volume-histogram of lung. Both figures show results from full patient specific 3D-RD calculation.

scatter, and collimator response. Collimator response includes septal penetration and scatter. The SPECT image counts were converted to units of activity by accounting for the detector efficiency and acquisition time. This quantification procedure, combined with image alignment, made it possible to follow the kinetics of each voxel. Using the CTs, which were acquired with each SPECT, each subsequent SPECT and CT image was aligned to the 27 hour 3-D image set. A voxel by voxel fit to an exponential expression was then applied to the aligned data set⁴⁰ to obtain the clearance half-time for each voxel.

To obtain mean absorbed dose, mean BED and EUD, as well as absorbed dose and BED-volume-histograms, voxels were assigned to either tumor or normal lung parenchyma using an activity threshold of 21% of highest activity value; this approach is the same as that used in reference 114.

The clinical example illustrates all of the elements that have an influence on absorbed dose at the voxel level. As shown on the CT scan (Fig. 5A), there is a highly variable density distribution in the lungs caused by the tumor infiltration of normal lung parenchyma. Coupled with the low lung density, this gives a density and tissue composition that includes air, lung parenchyma and tumor (which was modeled as soft tissue). As shown in Figures 5B and C, the activity and clearance kinetics of ¹³¹I are also variable over the lung volume. These 2 data sets were used to calculate the cumulated activity images shown in Figure 5D.

Figures 6 and 7 depict the results obtained with the radiobiological modeling capabilities of 3D-RD. Figure 6 depicts a parametric image of BED values. Within this image the spotty areas of highest dose are areas where high activity and low

density overlap. In Fig. 7a, normalized (so that the area under the curve is equal to 1) DVH and BED DVH (BVH) are shown for tumor voxels. The near superimposition of DVH and BVH suggests that dose rate will have a minimal impact on tumor response in this case. Figure 7b depicts the normalized BVH for normal lung parenchyma. The DVH and BVH are given in Gy and reflect the predicted doses resulting from the administered therapeutic activity of 1.32 GBq (35.6 mCi) of ¹³¹I. These plots may be used to derive EUD values. Mean absorbed dose, mean BED, and EUD are summarized in Table 4. The EUD value for tumor, which accounts for the effect of a nonuniform dose distribution, was approximately 43% of the mean absorbed dose. This reduction brings the absorbed dose to a range that is not likely to lead to a complete response using a single administration of activity. The analysis demonstrates the impact of dose nonuniformity on the potential efficacy of a treatment.

Future Implementations

The ability to translate parametric absorbed dose images from radionuclide therapy into BED images that can be compared with or added to BED images from external radiotherapy will make it possible to combine these two treatment modalities so that external radiotherapy planning can account for the dose-distribution arising from targeted radionuclide therapy.

Advances in biological imaging may be expected to provide information regarding the spatial variability of radiosensitivity within a tumor and such information could then be incorporated into the radiobiological modeling scheme described above by replacing the assumption of single-valued α , β , and μ parameters with voxel specific or subregion-specific values.

Routine implementation of the internal dosimetry methodology outlined in this work will require additional imaging and patient time. Given the attendant logistical and financial costs, a demonstrated improvement in patient care should be

Table 4 Summary of Results from the Clinical 3D-RD Calculation

	Tumor (Gy)	Lungs (Gy)
Mean absorbed dose	57.7	9.5
Mean BED	58.5	9.8
EUD	25.0	8.3

a prerequisite for the adoption of such highly patient-specific internal dosimetry.

References

1. Goldenberg DM: Targeted therapy of cancer with radiolabeled antibodies. *J Nucl Med* 43:693-713, 2002
2. Berndorff D, Borkowski S, Sieger S, et al: Radioimmunotherapy of solid tumors by targeting extra domain B fibronectin: Identification of the best-suited radioimmunoconjugate. *Clin Cancer Res* 11:7053S-7063S, 2005
3. Scott AM, Wiseman G, Welt S, et al: A phase I dose-escalation study of sibtrotuzumab in patients with advanced or metastatic fibroblast activation protein-positive cancer. *Clin Cancer Res* 9:1639-1647, 2003
4. Chiavassa S, Aubineau L, Bitar A, et al: Validation of a personalized dosimetric evaluation tool (Oedipe) for targeted radiotherapy based on the Monte Carlo MCNPX code. *Phys Med Biol* 51:601-616, 2006
5. Flux GD, Webb S, Ott RJ, et al: Three-dimensional dosimetry for intraliesional radionuclide therapy using mathematical modeling and multimodality imaging. *J Nucl Med* 38:1059-1066, 1997
6. Furhang EE, Chui CS, Kolbert KS, et al: Implementation of a Monte Carlo dosimetry method for patient-specific internal emitter therapy. *Med Phys* 24:1163-1172, 1997
7. Kolbert KS, Sgouros G, Scott AM, et al: Implementation and evaluation of patient-specific three-dimensional internal dosimetry. *J Nucl Med* 38:301-308, 1997
8. Behr TM, Sharkey RM, Sgouros G, et al: Overcoming the nephrotoxicity of radiometal-labeled immunoconjugates: improved cancer therapy administered to a nude mouse model in relation to the internal radiation dosimetry. *Cancer* 80:2591-2610, 1997 (suppl)
9. Tagesson M, Ljungberg M, Strand SE: A Monte-Carlo program converting activity distributions to absorbed dose distributions in a radionuclide treatment planning system. *Acta Oncol* 35:367-372, 1996
10. Sgouros G, Kolbert KS, Zaidi H: The three-dimensional internal dosimetry software package, 3D-ID. Therapeutic Applications of Monte Carlo Calculations in Nuclear Medicine. Philadelphia, Institute of Physics, 2002
11. Guy MJ, Flux GD, Papavasileiou P, et al: RMDP: A dedicated package for ¹³¹I SPECT quantification, registration and patient-specific dosimetry. *Cancer Biother Radiopharm* 18:61-69, 2003
12. Johnson TK, McClure D, McCourt S: MABDOSE. I: Characterization of a general purpose dose estimation code. *Med Phys* 26:1389-1395, 1999
13. Johnson TK, McClure D, McCourt S: MABDOSE. II: Validation of a general purpose dose estimation code. *Med Phys* 26:1396-1403, 1999
14. Liu A, Williams LE, Wong JY, et al: Monte Carlo-assisted voxel source kernel method (MAVSK) for internal beta dosimetry. *Nucl Med Biol* 25:423-433, 1998
15. Clairand I, Ricard M, Gouriou J, et al: DOSE3D: EGS4 Monte Carlo code-based software for internal radionuclide dosimetry. *J Nucl Med* 40:1517-1523, 1999
16. Yoriyaz H, Stabin MG, dos SA: Monte Carlo MCNP-4B-based absorbed dose distribution estimates for patient-specific dosimetry. *J Nucl Med* 2001;42:662-669
17. Yoriyaz H, dos SA, Stabin MG, et al: Absorbed fractions in a voxel-based phantom calculated with the MCNP-4B code. *Med Phys* 27:1555-1562, 2000
18. Descalle MA, Hartmann Siantar CL, Dauffy L, et al: Application of MINERVA Monte Carlo simulations to targeted radionuclide therapy. *Cancer Biother Radiopharm* 18:71-79, 2003
19. Bolch WE, Bouchet LG, Robertson JS, et al: MIRDOSE pamphlet No. 17: The dosimetry of nonuniform activity distributions—radionuclide S values at the voxel level. Medical Internal Radiation Dose Committee. *J Nucl Med* 1999;40:115-365
20. Snyder WS, Ford MR, Warner GG: Estimates of Specific Absorbed Fractions for Photon Sources Uniformly Distributed in Various Organs of a Heterogeneous Phantom. New York, The Society of Nuclear Medicine, 1978
21. Snyder WS, Ford MR, Warner GG, Watson SB. "S" Absorbed Dose Per Unit Cumulated Activity for Selected Radionuclides and Organs. MIRDO Pamphlet No. 11. New York, Society of Nuclear Medicine, 1975
22. Stabin MG. MIRDOSE: Personal computer software for internal dose assessment in nuclear medicine. *J Nucl Med* 37:538-546, 1996
23. Stabin MG, Sparks RB. OLINDA: PC-based software for biokinetic analysis and internal dose calculations in nuclear medicine. *J Nucl Med* 2003;44:103P
24. Stabin MG, Sparks RB, Crowe EB, et al: Olinda/Exm 1.0 and Radar. *Eur J Nucl Med Mol Imaging* 31:S471-S471, 2004
25. Aubineau-Laniece I, de Carlan L, Clairand I, et al: Current developments at IRSN on computational tools dedicated to assessing doses for both internal and external exposure. *Radiat Protection Dosimetry* 115:522-529, 2005
26. Chiavassa S, Bardies M, Guiraud-Vitoux F, et al: OEDIPE: A personalized dosimetric tool associating voxel-based models with MCNPX. *Cancer Biother Radiopharm* 20:325-332, 2005
27. Ferrer L, Chouin N, Bitar A, et al: Implementing dosimetry in GATE: Dose-point kernel validation with GEANT4 4.8.1. *Cancer Biother Radiopharm* 22:125-129, 2007
28. Visvikis D, Bardies M, Chiavassa S, et al: Use of the GATE Monte Carlo package for dosimetry applications. *Nucl Instr Methods Phys Res Sect A* 569:335-340, 2006
29. Descalle MA, Siantar CH, Walling R: Validation of an internal source model in the PEREGRINE system for targeted radionuclide therapy. *Med Phys* 29:1234-1235, 2002
30. Siantar CLH, Walling RS, Daly TP, et al: Description and dosimetric verification of the PEREGRINE Monte Carlo dose calculation system for photon beams incident on a water phantom. *Med Phys* 28:1322-1337, 2001
31. Zheng Z, Cardarelli G, Shearer D, et al: Peregrine as a verification tool of Corvus treatment planning system. *Med Phys* 29:1231-1232, 2002
32. Ljungberg M, Sjogreen K, Liu X, et al: A 3-dimensional absorbed dose calculation method based on quantitative SPECT for radionuclide therapy: Evaluation for ¹³¹I using monte carlo simulation. *J Nucl Med* 43:1101-1109, 2002
33. Ljungberg M, Frey E, Sjogreen K, et al: 3D absorbed dose calculations based on SPECT: Evaluation for ¹¹¹In-90Y therapy using Monte Carlo simulations. *Cancer Biother Radiopharm* 18:99-107, 2003
34. Sgouros G, Barest G, Thekkumthala J, et al: Treatment planning for internal radionuclide therapy: Three-dimensional dosimetry for non-uniformly distributed radionuclides. *J Nucl Med* 31:1884-1891, 1990
35. Mohan R, Barest G, Brewster LJ, et al: A comprehensive three-dimensional radiation treatment planning system. *Int J Radiat Oncol Biol Phys* 15:481-495, 1988
36. Sgouros G, Chiu S, Pentlow KS, et al: Three-dimensional dosimetry for radioimmunotherapy treatment planning. *J Nucl Med* 34:1595-1601, 1993
37. Baechler S, Hobbs RF, Prideaux AR, et al: Extension of the biological effective dose to the MIRDO schema and possible implications in radionuclide therapy dosimetry. *Med Phys* 35:1123-1134, 2008
38. Sgouros G, Squeri S, Ballangrud AM, et al: Patient-specific, 3-dimensional dosimetry in non-Hodgkin's lymphoma patients treated with ¹³¹I-anti-B1 antibody: Assessment of tumor dose-response. *J Nucl Med* 44:260-268, 2003
39. Kolbert KS, Sgouros G, Scott AM, et al: Dose-volume histogram representation of patient dose distribution in 3-dimensional internal dosimetry. *J Nucl Med* 35:P123-P124, 1994
40. Sgouros G, Kolbert KS, Sheikh A, et al: Patient-specific dosimetry for ¹³¹I thyroid cancer therapy using ¹²⁴I PET and 3-dimensional-internal dosimetry (3D-ID) software. *J Nucl Med* 45:1366-1372, 2004
41. Kolbert KS, Pentlow KS, Pearson JR, et al: Prediction of absorbed dose to normal organs in thyroid cancer patients treated with ¹³¹I by use of ¹²⁴I PET and 3-dimensional internal dosimetry software. *J Nucl Med* 48:143-149, 2007
42. Prideaux AR, Song H, Hobbs RF, et al: Three-dimensional radiobiologic dosimetry: Application of radiobiologic modeling to patient-

- specific 3-dimensional imaging-based internal dosimetry. *J Nucl Med* 48:1008-1016, 2007
43. Pentlow KS, Graham MC, Lambrecht RM, et al: Quantitative imaging of iodine-124 with PET. *J Nucl Med* 37:1557-1562, 1996
 44. Ljungberg M, Strand SE, King MA. Monte Carlo Calculations in Nuclear Medicine. Bristol, Institute of Physics Publishing, 1998
 45. Zaidi H, Sgouros G: Therapeutic Applications of Monte Carlo Calculations in Nuclear Medicine. Philadelphia, Institute of Physics Publishing, 2003
 46. Jaszczak RJ, Coleman RE, Whitehead FR: Physical factors affecting quantitative measurements using camera-based single photon-emission computed-tomography (SPECT). *IEEE Trans Nucl Sci* 28:69-80, 1981
 47. Jaszczak RJ, Greer KL, Floyd CE, et al: Improved SPECT quantification using compensation for scattered photons. *J Nucl Med* 25:893-900, 1984
 48. Jaszczak RJ, Whitehead FR, Lim CB, et al: Lesion detectability of rotating camera-based single photon-emission computed-tomography (SPECT). *J Nucl Med* 22:39-39, 1981
 49. Lechner PK, Koral KF, Jaszczak RJ, et al: An overview of imaging techniques and physical aspects of treatment planning in radioimmunotherapy. *Med Phys* 20:569-577, 1993
 50. Almquist H, Palmer J, Ljungberg M, et al: Quantitative SPECT by attenuation correction of the projection set using transmission data: Evaluation of a method. *Eur J Nucl Med* 16:587-594, 1990
 51. Dewaraja YK, Ljungberg M, Majumdar A, et al: A parallel Monte Carlo code for planar and SPECT imaging: Implementation, verification and applications in I-131 SPECT. *Comput Methods Programs Biomed* 67:115-124, 2002
 52. Ljungberg M, King MA, Hademenos GJ, et al: Comparison of four scatter correction methods using Monte Carlo simulated source distributions. *J Nucl Med* 35:143-151, 1994
 53. Ljungberg M, Strand SE: Attenuation correction in SPECT based on transmission studies and Monte Carlo simulations of build-up functions. *J Nucl Med* 31:493-500, 1990
 54. Ljungberg M, Strand SE: Scatter and attenuation correction in SPECT using density maps and Monte Carlo simulated scatter functions. *J Nucl Med* 31:1560-1567, 1990
 55. Ljungberg M, Strand SE: Attenuation and scatter correction in SPECT for sources in a nonhomogeneous object: A Monte Carlo study. *J Nucl Med* 32:1278-1284, 1991
 56. Sjogreen K, Ljungberg M, Strand SE: An activity quantification method based on registration of CT and whole-body scintillation camera images, with application to I-131. *J Nucl Med* 43:972-982, 2002
 57. Sjogreen K, Ljungberg M, Strand SE: Parameters influencing volume and activity quantitation in SPECT. *Acta Oncol* 35:323-330, 1996
 58. Beekman FJ, Kamphuis C, Frey EC: Scatter compensation methods in 3D iterative SPECT reconstruction: A simulation study. *Phys Med Biol* 42:1619-1632, 1997
 59. de Jong HW, Wang WT, Frey EC, et al: Efficient simulation of SPECT down-scatter including photon interactions with crystal and lead. *Med Phys* 29:550-560, 2002
 60. Du Y, Frey EC, Wang WT, et al: Combination of MCNP and SimSET for Monte Carlo simulation of SPECT with medium- and high-energy photons. *IEEE Trans Nucl Sci* 49:668-674, 2002
 61. Frey EC, Tsui BMW, Gullberg GT: Improved estimation of the detector response function for converging beam collimators. *Phys Med Biol* 43:941-950, 1998
 62. He B, Du Y, Song X, et al: A Monte Carlo and physical phantom evaluation of quantitative In-111 SPECT. *Phys Med Biol* 50:4169-4185, 2005
 63. He B, Frey EC: Comparison of conventional, model-based quantitative planar, and quantitative SPECT image processing methods for organ activity estimation using In-111 agents. *Phys Med Biol* 51:3967-3981, 2006
 64. He B, Wahl R, Du Y, et al: Comparison of residence time estimation methods for radioimmunotherapy dosimetry and treatment planning: Monte Carlo simulation studies. *IEEE Trans Med Imaging* 27:521-530, 2008
 65. Kadmas DJ, Frey EC, Tsui BM: Simultaneous technetium-99m/thallium-201 SPECT imaging with model-based compensation for cross-contaminating effects. *Phys Med Biol* 44:1843-1860, 1999
 66. Segars WP, Tsui BM, Lalush DS, et al: Development and application of the new dynamic Nurbs-based cardiac-torso (NCAT) phantom. *J Nucl Med* 42:7p, 2001 (abstr)
 67. Lewellen T, Harrison R, Vannoy S: The SimSET program, in Monte Carlo calculations in nuclear medicine: applications in diagnostic imaging, in: Ljungberg M, Strand S-E, King M (eds): Monte Carlo Calculations in Nuclear Medicine. Applications in Diagnostic Imaging. Bristol, UK, Institute of Physics, 1998, pp 77-92
 68. Du Y, Tsui BMW, Frey EC: Model-based compensation for quantitative I-123 brain SPECT imaging. *Phys Med Biol* 51:1269-1282, 2006
 69. Frey EC, He B, Sgouros G, et al: Comparison of planar, quantitative SPECT, and combined planar-quantitative SPECT organ residence time estimation methods for targeted radionuclide therapy dosimetry. *J Nucl Med* 2004;45 46P (abstr)
 70. He B, Frey EC, Sgouros G, et al: Comparison of conventional planar, quantitative planar, quantitative SPECT and combined planar-SPECT organ residence time estimation methods for targeted radionuclide therapy dosimetry. *J Nucl Med* 46:26P-26P, 2005
 71. He B, Frey EC, Tsui BM: Comparison and validation of conjugate view planar, model-based quantitative planar, and quantitative SPECT methods for whole organ activity estimation. *J Nucl Med* 46:50P-50P, 2005
 72. Dewaraja YK, Wilderman SJ, Ljungberg M, et al: Accurate dosimetry in I-131 radionuclide therapy using patient-specific, 3-dimensional methods for SPECT reconstruction and absorbed dose calculation. *J Nucl Med* 46:840-849, 2005
 73. O'Donoghue JA, Sgouros G, Divigi CR, et al: Single-dose versus fractionated radioimmunotherapy: Model comparisons for uniform tumor dosimetry. *J Nucl Med* 41:538-547, 2000
 74. O'Donoghue JA: Implications of nonuniform tumor doses for radioimmunotherapy. *J Nucl Med* 40:1337-1341, 1999
 75. Roberson PL, Heidorn DB, Kessler ML, et al: Three-dimensional reconstruction of monoclonal antibody uptake in tumor and calculation of beta dose-rate nonuniformity. *Cancer* 73:912-918, 1994 (3 suppl)
 76. Muthuswamy MS, Roberson PL, Ten Haken RK, et al: A quantitative study of radionuclide characteristics for radioimmunotherapy from 3D reconstructions using serial autoradiography. *Int J Radiat Oncol Biol Phys* 35:165-172, 1996
 77. Flynn AA, Pedley RB, Green AJ, et al: The nonuniformity of antibody distribution in the kidney and its influence on dosimetry. *Radiat Res* 159:182-189, 2003
 78. Howell RW, Rao DV, Sastry KS: Macroscopic dosimetry for radioimmunotherapy: nonuniform activity distributions in solid tumors. *Med Phys* 16:66-74, 1989
 79. Humm JL, Cobb LM: Nonuniformity of tumor dose in radioimmunotherapy. *J Nucl Med* 31:75-83, 1990
 80. Flynn AA, Pedley RB, Green AJ, et al: Optimizing radioimmunotherapy by matching dose distribution with tumor structure using 3D reconstructions of serial images. *Cancer Biother Radiopharm* 16:391-400, 2001
 81. Flynn AA, Pedley RB, Green AJ, et al: Antibody and radionuclide characteristics and the enhancement of the effectiveness of radioimmunotherapy by selective dose delivery to radiosensitive areas of tumour. *Int J Radiat Biol* 78:407-415, 2002
 82. Hall EJ: Radiation dose-rate: a factor of importance in radiobiology and radiotherapy. *Br J Radiol* 45:81-97, 1972
 83. Barendsen GW: Dose fractionation, dose rate and iso-effect relationships for normal tissue responses. *Int J Radiat Oncol Biol Phys* 8:1981-1997, 1982
 84. Fowler JF: The linear-quadratic formula and progress in fractionated radiotherapy. *Br J Radiol* 62:679-694, 1989
 85. Rao DV, Howell RW: Time-dose-fractionation in radioimmunotherapy: Implications for selecting radionuclides. *J Nucl Med* 34:1801-1810, 1993
 86. Howell RW, Goddu SM, Rao DV: Application of the linear-quadratic

- model to radioimmunotherapy: Further support for the advantage of longer-lived radionuclides. *J Nucl Med* 35:1861-1869, 1994
87. Mayer R, Dillehay LE, Shao Y, et al: Direct measurement of intratumor dose-rate distributions in experimental xenografts treated with ⁹⁰Y-labeled radioimmunotherapy. *Int J Radiat Oncol Biol Phys* 32:147-157, 1995
 88. Akabani G, Cokgor I, Coleman RE, et al: Dosimetry and dose-response relationships in newly diagnosed patients with malignant gliomas treated with iodine-131-labeled anti-tenascin monoclonal antibody 81C6 therapy. *Int J Radiat Oncol Biol Phys* 46:947-958, 2000
 89. DeNardo GL, Schlom J, Buchsbaum DJ, et al: Rationales, evidence, and design considerations for fractionated radioimmunotherapy. *Cancer* 94:1332-1348, 2002 (4 suppl)
 90. Flynn AA, Pedley RB, Green AJ, et al: Effectiveness of radiolabelled antibodies for radio-immunotherapy in a colorectal xenograft model: a comparative study using the linear-quadratic formulation. *Int J Radiat Biol* 77:507-517, 2001
 91. Shen S, Duan J, Meredith RF, et al: Model prediction of treatment planning for dose-fractionated radioimmunotherapy. *Cancer* 94:1264-1269, 2002 (4 suppl)
 92. Behr TM, Memtsoudis S, Sharkey RM, et al: Experimental studies on the role of antibody fragments in cancer radio-immunotherapy: Influence of radiation dose and dose rate on toxicity and anti-tumor efficacy. *Int J Cancer* 77:787-795, 1998
 93. Bodey RK, Evans PM, Flux GD: Application of the linear-quadratic model to combined modality radiotherapy. *Int J Radiat Oncol Biol Phys* 59:228-241, 2004
 94. Bodey RK, Flux GD, Evans PM: Combining dosimetry for targeted radionuclide and external beam therapies using the biologically effective dose. *Cancer Biother Radiopharm* 18:89-97, 2003
 95. Zhu H, Jain RK, Baxter LT: Tumor pretargeting for radioimmunodetection and radioimmunotherapy. *J Nucl Med* 39:65-76, 1998
 96. Atwell JL, Breheny KA, Lawrence LJ, et al: scFv multimers of the anti-neuraminidase antibody NC10: length of the linker between VH and VL domains dictates precisely the transition between diabodies and triabodies. *Protein Eng* 12:597-604, 1999
 97. Lawrence LJ, Kortt AA, Iliades P, et al: Orientation of antigen binding sites in dimeric and trimeric single chain Fv antibody fragments. *FEBS Lett* 425:479-484, 1998
 98. Le Gall F, Kipriyanov SM, Moldenhauer G, et al: Di-, tri- and tetrameric single chain Fv antibody fragments against human CD19: Effect of valency on cell binding. *FEBS Lett* 453:164-168, 1999
 99. De Jong M, Valkema R, Jamar F, et al: Somatostatin receptor-targeted radionuclide therapy of tumors: Preclinical and clinical findings. *Semin Nucl Med* 32:133-140, 2002
 100. De Jong M, Breeman WA, Bernard HF, et al: Therapy of neuroendocrine tumors with radiolabeled somatostatin- analogues. *Q J Nucl Med* 43:356-366, 1999
 101. McEwan AJ: Palliative therapy with bone seeking radiopharmaceuticals. *Cancer Biother Radiopharm* 13:413-426, 1998
 102. Giralt S, Bensinger W, Goodman M, et al: Ho-166-DOTMP plus melphalan followed by peripheral blood stem cell transplantation in patients with multiple myeloma: results of two phase 1/2 trials. *Blood* 102:2684-2691, 2003
 103. Farhanghi M, Holmes RA, Volkert WA, et al: Samarium-153-EDTMP: Pharmacokinetic, toxicity and pain response using an escalating dose schedule in treatment of metastatic bone cancer. *J Nucl Med* 33:1451-1458, 1992
 104. Cohen EP, Moulder JE, Robbins ME: Radiation nephropathy caused by yttrium 90. *Lancet* 358:1102-1103, 2001
 105. Otte A, Weiner SM, Cybulla M: Is radiation nephropathy caused by yttrium-90? *Lancet* 359:979, 2002
 106. Boerman OC, Oyen WJ, Corstens FH: Between the Scylla and Charybdis of peptide radionuclide therapy: Hitting the tumor and saving the kidney. *Eur J Nucl Med* 28:1447-1449, 2001
 107. Breitz H, Wendt R, Stabin M, et al: Dosimetry of high dose skeletal targeted radiotherapy (STR) with (166)Ho-DOTMP. *Cancer Biother Radiopharm* 18:225-230, 2003
 108. Furhang EE, Chui CS, Sgouros G: A Monte Carlo approach to patient-specific dosimetry. *Med Phys* 23:1523-1529, 1996
 109. Dale R, Carabe-Fernandez A: The radiobiology of conventional radiotherapy and its application to radionuclide therapy. *Cancer Biother Radiopharm* 20:47-51, 2005
 110. Zaider M, Hanin L: Biologically-equivalent dose and long-term survival time in radiation treatments. *Phys Med Biol* 52:6355-6362, Oct 2007.
 111. Lucas JN, Tenjin T, Straume T, et al: Rapid human chromosome aberration analysis using fluorescence in situ hybridization. *Int J Radiat Biol* 56:35-44, 1989
 112. Millar WT: Application of the linear-quadratic model with incomplete repair to radionuclide directed therapy. *Br J Radiol* 64:242-251, 1991
 113. Loevinger R, Budinger TF, Watson EE: *MIRD Primer for Absorbed Dose Calculations*, Revised Edition. New York, The Society of Nuclear Medicine, Inc., 1991
 114. Song H, He B, Prideaux A, et al: Lung dosimetry for radioiodine treatment planning in the case of diffuse lung metastases. *J Nucl Med* 47:1985-1994, 2006
 115. Frey EC, Gilland KL, Tsui BM: Application of task-based measures of image quality to optimization and evaluation of three-dimensional reconstruction-based compensation methods in myocardial perfusion SPECT. *IEEE Trans Med Imaging* 21:1040-1050, 2002